Coherent manipulation of a molecular Ln-based nuclear qudit coupled to an electron qubit

Riaz Hussain[1], Giuseppe Allodi[1], Alessandro Chiesa[1], Elena Garlatti[1,2], Dmitri Mitcov[3], Andreas Konstantatos[3], Kasper S. Pedersen[3,4], Roberto De Renzi[1], Stergios Piligkos[3] and Stefano Carretta[1,5]

[1]Dipartimento di Scienze Matematiche, Fisiche e Informatiche, Università di Parma, I-43124 Parma, Italy.
[2]ISIS Facility, Rutherford Appleton Laboratory, OX11 0QX Didcot, United Kingdom.
[3]Department of Chemistry, University of Copenhagen, DK-2100 Copenhagen, Denmark.
[4]Department of Chemistry, Technical University of Denmark, DK-2800, Kgs. Lyngby, Denmark.
[5]UdR Parma, INSTM, I-43124 Parma, Italy.

Supporting Information

1. Synthesis and characterizations

Single-crystals of [Yb(trensal)] doped into the isostructural [Lu(trensal)] at 2% (**1**) were synthesized and grown over several weeks following a previously described method for Er(trensal) [S1] that employed a mixture of $Yb(CF_3SO_3)_3{\cdot}9H_2O$ (1 mol%) and $Lu(CF_3SO_3)_3{\cdot}9H_2O$ (99 mol%), respectively.

The identity of the single-crystals was confirmed by single-crystal and powder (crashed single-crystals) X-ray diffraction experiments. The obtained results (trigonal $P\bar{3}c1$ space group) were consistent with previously reported analyses [S2]. Crystallographic data for [Yb(trensal)] can be obtained free of charge from The Cambridge Crystallographic Data Centre (CCDC) via www.ccdc.cam.ac.uk/data_request/cif. The structure is registered in CCDC with number 1044477.

The actual doping concentration of Yb was determined by Inductively Coupled Plasma Mass Spectrometry (ICP-MS; Bruker Aurora Elite). The instrument was tuned prior to measurement and external calibration was performed using calibration points spanning the range of concentrations encountered in the samples. Nitric acid used was TraceSelect grade, reference material was provided by Inorganic Ventures. The sample was prepared by dissolution of a single crystal (of the same crystallization batch as the one providing the crystal for the experiments presented) with a mass of 0.867 mg in 2% nitric acid (dissolved in 50 mL from which 0.125 mL was diluted to 50 mL). The analysis afforded the mass percentages of 0.59% and 27.16% for Yb and Lu, respectively. This gives a Yb/Lu ratio of 2.14%. For comparison, the theoretical mass percentages are calculated from $Yb_{0.02}Lu_{0.98}C_{27}H_{27}N_4O_3$ to be 0.55% and 27.20%, for Yb and Lu, respectively. ICP-MS sample preparation and analysis were performed at the Department of Chemistry, University of Copenhagen.

2. Experimental details

The NMR experiments were performed by means of a home-built broadband NMR spectrometer optimized for magnetism, named 'HyReSpect' [S3] in a Maglab EXA (Oxford Instruments) 0-9T variable field superconducting cold-bore magnet equipped with a helium flow variable temperature insert. The HyReSpect spectrometer features a flat frequency response over the 8-800MHz frequency span, a passband of ±3MHz around its working frequency, a fast-repeating digitizer with a maximum sampling rate of 25Msample/s, and timing provided by a microcontroller clocked at 84MHz, capable of triggering variable pulses from a minimum length of 95ns (8 clock cycles) in steps of 1 clock cycle. All these characteristics make the instrument suitable to excite and detect spin echoes with very short pulses and pulse delays over a wide frequency range, as required by the present experiments. The radio frequency (rf) pulses were amplified by a linear pulse power amplifier to levels of 0.2-20W, depending on the field-dependent enhancement (see below), and fed into the NMR probehead hosted by the cryostat. The probehead consists in a lumped LC resonant circuit with an interchangeable sample coil made of two or just one loop, depending on the target frequencies and sample mounting, yielding a typical Q-factor in the order of 200 at low temperature, and providing a tuning range of more than one octave with a given coil. All measurements were carried out at base temperature by pumping from a small liquid helium

bath in the cryostat by means of a 300l/min Roots pump in a steady-state, allowing stable operation at 1.4K with reliable sample thermalization.

2.1 Hahn echo sequences

The NMR spectra were recorded by exciting and detecting spin echoes by a sequence of two equal pulses of 500ns duration and power optimized for maximum signal. This condition corresponds to a nutation angle of 2π/3 for each pulse [S4]. We have preferred this sequence to the standard π/2− π echo sequence, in principle the optimal one, due to the fact that the efficiency gain of the latter vanishes in the case of very broad lines typical of magnetic systems, whereby just a portion of the spectrum, proportional to the Fourier transform of the longer pulse, is excited by the echo. Conversely, an equal-pulse sequence is favourable in the case of very short T_2 due to its shorter overall duration, and it is more tolerant to an excessive rf power level due to imperfect pulse calibration.
The spectral width effectively observed by each spin echo was limited by the Fourier transform of a pulse (±1MHz wide), further filtered by the finite bandwidth of the tuned probehead. This was comparable or slightly smaller than the width of the individual resonance lines. Each resonance peak was therefore reconstructed by merging the Fourier transforms of a few echoes (typically 5) recorded with a frequency offset of 200-300 kHz relative to each other.

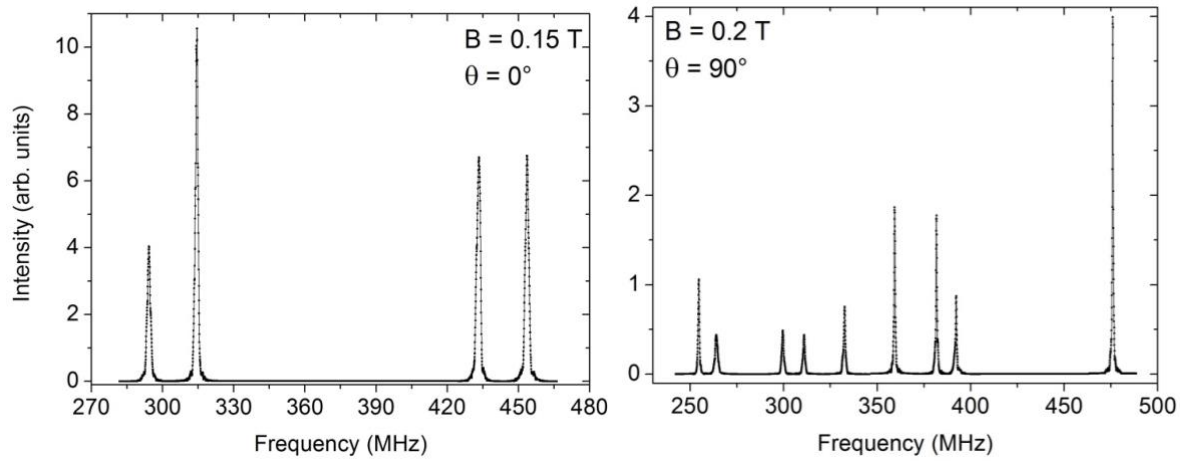

Fig. S1: Two examples of NMR spectra of (1) as a function of frequency, measured at T = 1.4 K for $\theta = 0°, 90°$ and B = 0.15, 0.2 T respectively.

The spin-spin relaxation rate $1/T_2$ was measured systematically for each line in various applied fields by recording spin echoes excited by the same pulse-τ-pulse sequence as for spectra, as a function of the delay τ. The echo amplitude, proportional to the component of the transverse magnetization precessing at the resonance frequency of a given line, exhibits a decay which is fitted to an exponential law with reasonable accuracy.

$$M(\tau) = M_0 e^{\frac{-2\tau}{T_2}}$$

The so-determined decay rate $1/T_2$ represents the homogeneous line-width Δω of the transition line, i.e. the intrinsic de-coherence time of the two levels involved in the transition solely due to irreversible processes. In all cases the homogenous line width was found to be much smaller than the observed spectral line width, which proves that the latter is essentially determined by static inhomogeneities.

By increasing the temperature, we expect a decrease of T_2, induced by the larger number of electronic spin flops due to the decrease of electronic spin polarization. Conversely, the role of neighboring nuclei should be substantially temperature independent. By further increasing the temperature, additional mechanisms are expected to raise, in particular spin-lattice relaxation which could lead to a stronger temperature dependence.

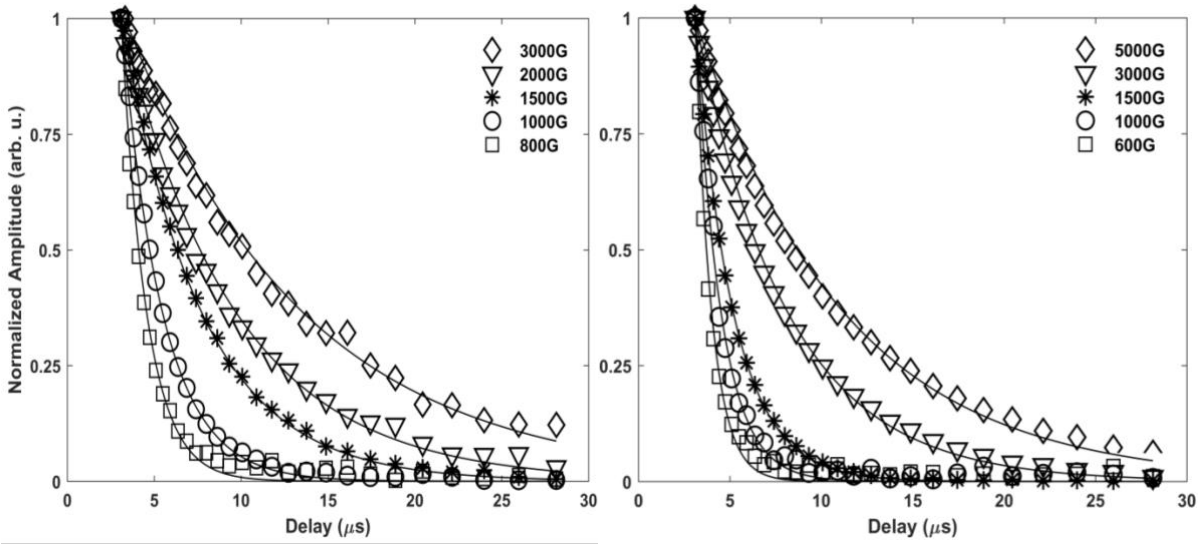

Fig. S2: Few examples of T_2 decay curves, measured as described above for $\theta = 0°, 81°$ orientations (respectively), at various values of B. Lines are the mono-exponential fits to the experimental data and a guide to the eye.

Rabi oscillation were produced by a ϕ-π echo sequence as described in the text, with the first pulse of variable duration producing a spin nutation by an angle ϕ, and a second well-calibrated π pulse refocusing the precessing spins in order to observe them after the receiver dead time (~2μs). The resulting echoes were Fourier-transformed, phase-corrected and analyzed in the frequency domain by picking the spectral amplitude of the echo at a fixed frequency shift. This analysis procedure compensates for the fact that at large ϕ values, corresponding to relatively small spectral widths irradiated by the first pulse, a fraction of nuclei of the inhomogeneously-broadened resonance line (namely, those with a shift larger than the spectral width of the pulse) are not effectively excited and do not participate in the echo.

2.2 CPMG

The Carr-Purcell-Meiboom-Gill (CPMG) pulse sequence consists in an initial $\pi/2$-τ -π echo sequence, followed by a train of N-1 π pulses at times 3τ , 5τ , ..., $(2N - 1)\tau$ from the initial $\pi/2$ pulse (here times are measured from pulse centre to pulse centre). The precessing spins excited by the first $\pi/2$ pulse, initially phase-coherent, are focused at a time 2τ where they produce a Hahn echo, and further refocused by the subsequent π pulses, giving rise to additional echoes centred at times 4τ , 6τ, ... $2N\tau$. Clearly, the whole echo profile originates from the bunch of spins initially tilted by the $\pi/2$ pulse, as these echoes do not overlap with the echoes possibly produced by the π pulses themselves, occurring (if π pulses are not perfectly calibrated) at odd times 3τ, 5τ , ... Phase coherence is therefore preserved over the

multiple echoes, except for dynamic T_2 processes leading to irreversible coherence loss, and the echo profile is expected to decay according to a law

$$M_n = M_0 e^{\frac{-2n\tau}{T_2}}$$

Experimentally, attention has to be paid to avoid a distortion of the decay profile due e.g. to uncalibrated π pulse. However, such a distortion may be compensated for by applying the π/2 pulse with a rf field H_1 along the x direction in the rotating frame, followed by either i) π pulses alternatingly along the ±x direction, or ii) π pulses along the y direction [S5]. We tried both the ±x and the y sequences, and checked the tolerance to pulse uncalibration by changing the rf output level by ±1, ±2 dB, obtaining the same CPMG echo profile in all cases.
The T_2 constant defined here is conceptually the same that could be measured by varying the delay in a single spin echo sequence. In liquids, however, the echo decay may be affected by spin diffusion, leading to a faster non-exponential decay $\boldsymbol{e^{-at^3}}$, while a slower exponential decay, governed by true T_2 processes, is recovered by a CPMG sequence with an arbitrarily small echo delay t. The CPMG sequence therefore gives rise to an extended spin coherence time. Although spin diffusion cannot be at play in the present system, we observed a qualitatively similar coherence enhancement effect by applying multiple pulses in a CPMG sequence. We believe that the enhancement in the observed coherence time could also arise from a dynamical effect induced by the multiple nutations of the CPMG sequence on the coupled nuclear-electronic moments, which might hinder electronic spin relaxation channels. Here the CPMG profile was modelled with a single-exponential decay (reported in Fig. 2 of the main text) up to 50 μs, while a slower component with a much longer T_2 emerges at long times.

2.3 Spin lattice nuclear relaxation

The spin lattice relaxation time T_1 is defined as $1/T_1=2W$, where W is the transition rate between two adjacent nuclear levels m_I, $m_I + 1$. In the simple case of a spin I=1/2 the so-defined $1/T_1$ coincides with the decay rate of the off-equilibrium longitudinal nuclear magnetization. With larger spins I and non-degenerate Zeeman transitions, however, the quantity accessed experimentally is the population difference of the level pair involved in the observed nuclear resonance, rather than the entire nuclear magnetization. Rate equations for the nuclear populations then lead to multi-exponential decay/recovery laws for each resonance even in the case of a single transition probability W [S5, S7], with up to 2I exponential components exhibiting enhanced rates 2W, 6W, 12W, 20W, 30W, ... and weights depending on the preparation (i.e. saturation) method for the nuclear ensemble, namely, whether just the populations of the observed transition are altered, or the preparation pulse sequence is long enough to allow for a recovery to thermal equilibrium for the other nuclear levels, or any intermediate case between the previous ones. Clearly, a detailed theoretical model, as well as a precise control of the initial conditions, would be required for an absolute quantitative determination of $1/T_1$. Here we can just provide an estimate for its order of magnitude as well as its relative dependence on the applied field.
Figures S3 show recovery curves for the polarization of a few selected transitions after a fast saturation of the resonance line, performed by a short pulse train of overall duration ~12μs.

Notoriously, the relative weight of the faster relaxing exponential components is enhanced by the fast saturation method [S6]. Nonetheless, it is clear from the figure that *i*) the slowest exponential components recover to their asymptotic values with characteristic times $t \leq T_1$ in the order of several ms, and *ii*) relaxation rates decrease with increasing applied field, as a consequence of field-induced decoupling of the nuclear and electronic spins. We can conclude therefore that spin-lattice relaxation takes place on a relatively long time scale and is not of concern for spin decoherence.

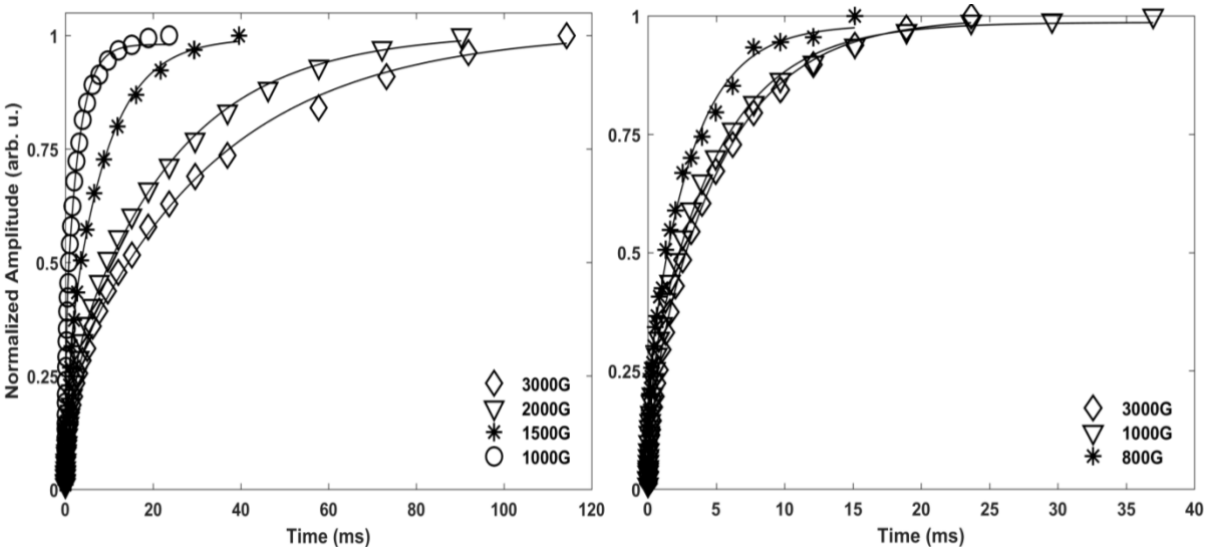

Fig. S3: Few examples of saturation recovery curves, measured as described above for $\theta = 0°$ orientation at various values of B. Black lines are fits to the experimental points by means of a bi-exponential law and a guide to the eye.

3. Spin Hamiltonian calculations

The parameters of the spin Hamiltonian for [Yb(trensal)] (Eq. (1) of the main text) have been determined from the positions of the peaks of the measured NMR spectra (see for instance Fig. S1 and Fig. 1 of the main text). From the comparison of our calculations with these data we have been able to determine only the absolute values of the hyperfine coefficients $A_\perp$ and $A_\parallel$. Indeed, transition frequencies don't depend on their signs, whose estimation would only be possible by studying the relative intensity of the NMR peaks. In our NMR experiments the intensities of the NMR peaks strongly depends on the experimental parameters (e.g. linear pulse power amplifier levels), which varied with both frequency and field in order to optimize the experimental conditions to detect each transition. Thus, we preserved the signs of both $A_\perp$ and $A_\parallel$ as determined by EPR [S2a].

The quadrupolar term p is essential to reproduce NMR data, while it was not possible to determine it from EPR measurements. Indeed, if p = 0 a variation of the angle θ between the applied magnetic field and the C_3 axis of the molecule only leads to rigid vertical shift of all the transition frequencies (at fixed B). Instead, non-uniform shifts are observed by changing the orientation from $\theta = 0°$ to $\theta = 81°$ and $\theta = 90°$ (see Fig. 1 of the main text).

3.1 Levels vs. field

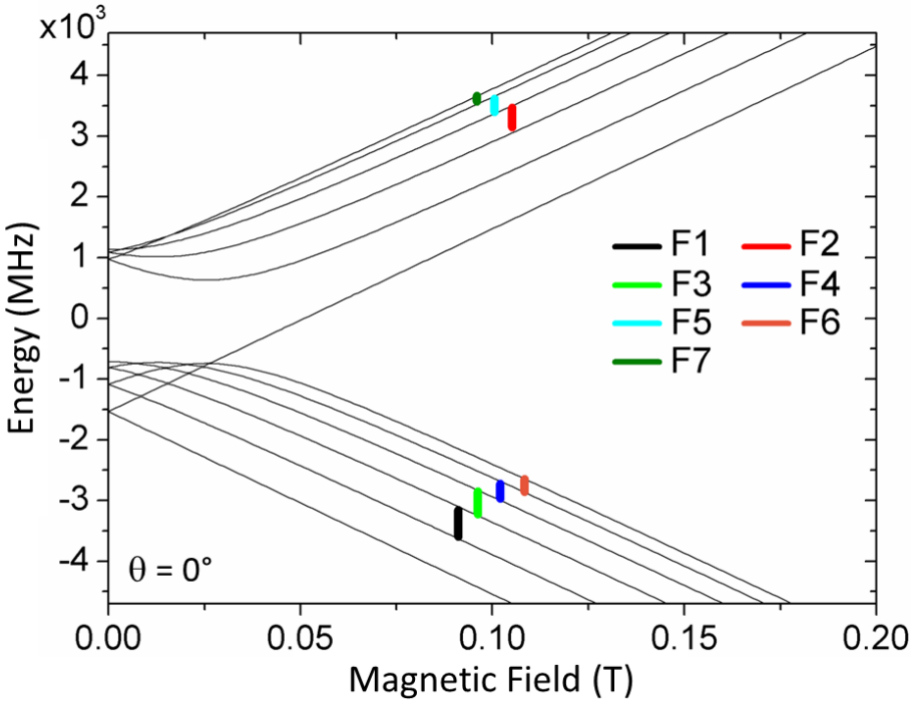

Fig. S4: Computed level diagram as a function of the applied field for $\theta = 0°$.

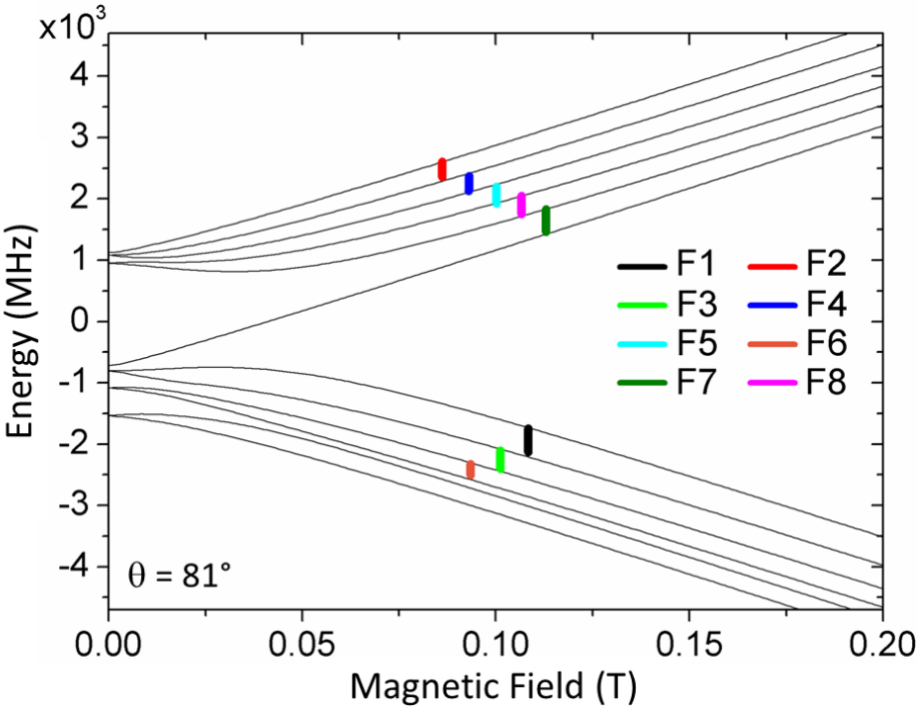

Fig. S5: Computed level diagram as a function of the applied field for $\theta = 81°$.

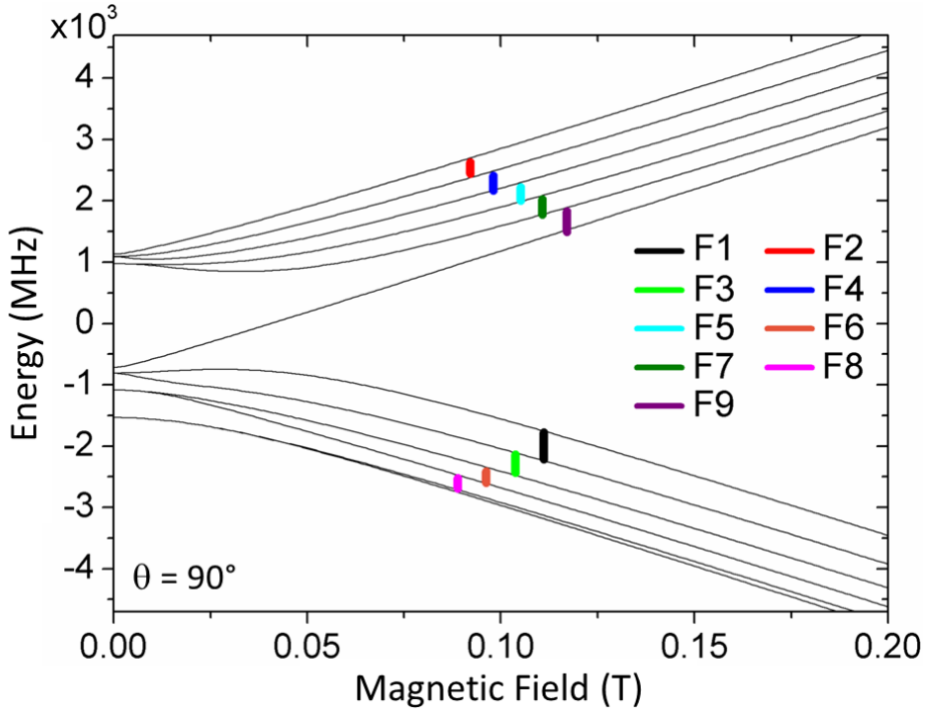

Fig. S6: Computed level diagram as a function of the applied field for $\theta = 90°$.

3.2 Electronic enhancement of nuclear transitions

We report here a more detailed analysis of the electron-nuclear mixing [Eq. (2) of the main text] and of the following enhancement of the Rabi frequency. We assume a static field applied along z and neglect nuclear quadrupolar interactions. In the limit $g\mu_B B > |A_\perp|$, we can obtain an analytical expression for the system wave-function corrected to first order in $A_\perp$:

$$|\psi_{m_S m_I}\rangle = |m_S, m_I\rangle \pm \frac{A_\perp \langle m_S \mp 1, m_I \pm 1 | S_x I_x + S_y I_y | m_S, m_I\rangle |m_S \mp 1, m_I \pm 1\rangle}{g_z \mu_B B + (m_I \pm 1/2) A_\parallel}$$
$$= |m_S, m_I\rangle \pm \frac{\alpha A_\perp}{g_z \mu_B B + (m_I \pm 1/2) A_\parallel} |m_S \mp 1, m_I \pm 1\rangle$$

where $\alpha = \langle m_I \pm 1 | I_x | m_I \rangle = \frac{1}{2}\sqrt{\frac{35}{4} - m_I(m_I \pm 1)}$ (close to 1) and $|m_S, m_I\rangle$ is the unperturbed wave-function.
The matrix element of the detected nuclear transitions is given by:

$$\langle \psi_{m_S m_I} | g_I \mu_N I_x + g_x \mu_B S_x | \psi_{m_S m_{I\pm1}} \rangle$$
$$= g_I \mu_N \langle m_I | I_x | m_I \pm 1\rangle \pm \frac{\alpha A_\perp}{g_z \mu_B B + (m_I \pm 1/2) A_\parallel} g_x \mu_B \langle m_S \mp 1 | S_x | m_S \rangle$$
$$= \alpha \left(g_I \mu_N \pm \frac{A_\perp g_x \mu_B}{2 g_z \mu_B B + (2 m_I \pm 1) A_\parallel} \right) \approx \alpha \left(g_I \mu_N \pm \frac{A_\perp}{2B} \right)$$

The last equality holds only for large magnetic fields and $g_x \approx g_z$.

4. Rabi oscillations

As reported in the main text, for sufficiently large powers the decay of the Rabi oscillations is dominated by inhomogeneities of the oscillating field (B_1). Following Ref. 53, we model the Rabi damping rate as

$$\tau^{-1} = \frac{1}{T_2} + mB_1$$

Where the first term is the measured T_2 of the examined transition while the second accounts for inhomogeneities of the oscillating field and is thus proportional to B_1.

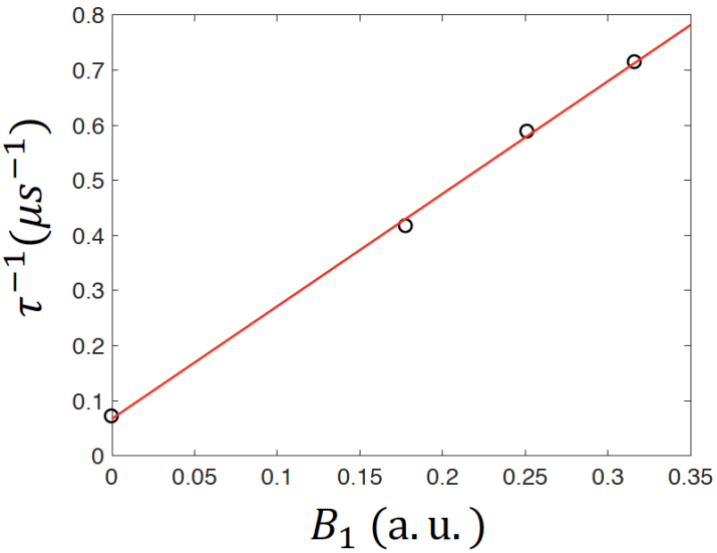

Fig. S7: Damping rate of the Rabi oscillations of transition F3 ($\theta = 0°$) reported in the main text, as a function of the oscillating field B_1.

Below we report the Rabi oscillations corresponding to transition F4 with two different values of the oscillating field, evidencing the monochromatic character of the oscillations (single peak in the Fourier transform, right panel) and the scaling of the Rabi frequency ν_R with B_1.

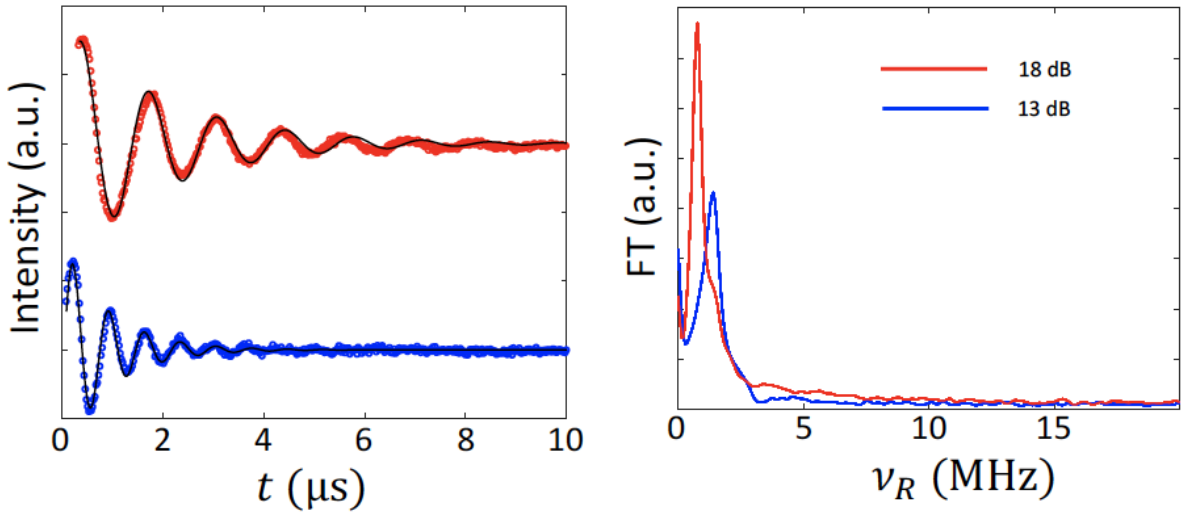

Fig. S8: Left: Rabi oscillations for transition F4, for two different attenuations (13 and 18 dB). Right: corresponding Fourier transforms of the signal, evidencing the monochromatic character of the oscillations.

5. Quantum Error Correction

Quantum error correction techniques are based on the redundant encoding of information. This implies embedding a quantum information unit (a qubit), belonging to a two-dimensional Hilbert space, into a larger one. Standard quantum error correction algorithms are based on *block-encoding* of the logical qubit into a set of several physical qubits (three at least) in order to extract the error syndrome by majority voting.
Here we pursue a different approach, i.e. we exploit the extra space available in the $d = 2I + 1$ dimensional Hilbert space of ^{173}Yb nucleus to obtain a *qudit-encoding* of the logical qubit. In particular, we show that a minimal scheme [S7] to detect and correct a single class of errors, either amplitude shifts or phase shifts, can be implemented.
The possible errors acting on a single qudit can be expanded in terms of a unitary operator basis with d^2 elements [S8], the "generalized Pauli operators":

$$X^a Z^b, \qquad a, b = 0,1, \dots, d-1$$

with

$$X|j\rangle = |j + 1 \bmod d\rangle$$
$$Z|j\rangle = e^{i\frac{2\pi}{d}j}\,|j\rangle$$

These operators represent the basic quantum errors which a quantum correcting code must correct [S7]. They can be distinguished into amplitude shifts X^a (discussed in the main text) and complementary phase shifts Z^b.
It can be shown [S7] that the smallest qudit which protects against a single amplitude (X) or phase (Z) shift is characterized by $d = 6$. In general, we need $d = 2(2k + 1)$ to correct k shifts. This should be compared with the corresponding exponential scaling of the Hilbert space dimension required by block-encoding $d = 2^{2k+1}$. Hence, block-encoding algorithms are exponentially more demanding than shift-resistant codes based on qudit-encoding.

In our physical system $|j\rangle$ are the nuclear levels. Following Ref. [S7], we re-label the qudit states according to $|m_S = -1/2, m_I\rangle \rightarrow \overline{|m_I + 5/2\rangle} = \overline{|0\rangle}, \overline{|1\rangle}, \overline{|2\rangle}, \overline{|3\rangle}, \overline{|4\rangle}, \overline{|5\rangle}$. The procedure reported in the text, based on encoding the generic state of the qubit $\alpha|0\rangle + \beta|1\rangle$ into $\alpha\overline{|1\rangle} + \beta\overline{|4\rangle}$, protects from an amplitude shift X. It is important to note that an analogous procedure in the conjugate basis allows one to protect the system from phase shifts. The encoded state in the conjugate basis is given by

$$\alpha\widetilde{|1\rangle} + \beta\widetilde{|4\rangle}$$

with

$$\widetilde{|l\rangle} = \frac{1}{\sqrt{6}} \sum_{j=0}^{5} e^{-i\frac{2\pi}{d}jl} \, \overline{|j\rangle}$$

After a possible phase shift has occurred, the inverse unitary transformation must be applied before performing error detection in the standard $\overline{|j\rangle}$ basis. While this could involve a complex sequence of control radio-frequency (rf) and microwave (mw) pulses, it is possible to implement any unitary transformation on the qudit [S9] with the present resources [S10].

The implementation of the amplitude/phase shift-resistant code requires the ability to implement X and Z operators within our setup [S8]. Since all transitions are well resolved, this can be achieved by exploiting the electronic spin as an auxiliary system and applying a sequence of mw and rf pulses.
In particular, at low temperatures (see below) only the $m_S = -1/2$ manifold is populated. Hence (see Fig. S9), we first (I) apply a mw π pulse resonant with the $|m_S = -1/2, m_I = 5/2\rangle \rightarrow |m_S = 1/2, m_I = 5/2\rangle$ gap to excite the $m_I = 5/2$ component of the wave-function. Then (II-VI) subsequent rf π pulses resonant with neighboring nuclear gaps are applied in parallel on both $m_S = -1/2$ and $m_S = 1/2$ manifolds. The final step consists of a mw π pulse resonant with the $|m_S = 1/2, m_I = -5/2\rangle \rightarrow |m_S = -1/2, m_I = -5/2\rangle$. This sequence implements the transformation

$$\sum_{m_I} a_{m_I} \left|m_S = -\frac{1}{2}, m_I\right\rangle \rightarrow \sum_{m_I} a_{m_I} \left|m_S = -\frac{1}{2}, m_I + 1\right\rangle$$

(with periodic boundary conditions) which corresponds to the X operator.

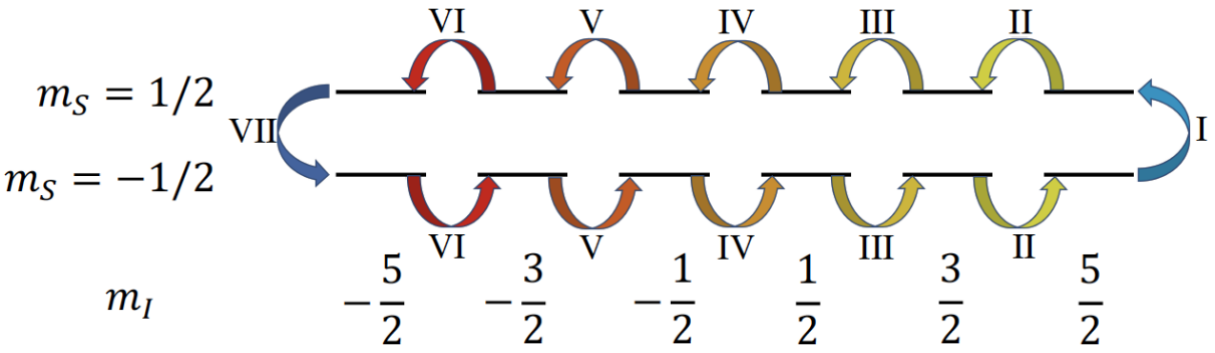

Fig. S9: Implementation of generalized X gate by a sequence of mw and rf π pulses. Numbers and colors (from light yellow to red) refer to the order in which pulses are applied.

Conversely, the Z operator, which adds a different phase to each component of the nuclear wave-function, is implemented by mw pulses semi-resonant with $|m_S = -1/2, m_I\rangle \leftrightarrow |m_S = 1/2, m_I\rangle$ gaps, applied in parallel to all the m_Is. Semi-resonant pulses are 2π pulses detuned from the target transition of an amount δ, which result in a phase $\varphi = \pi - \pi \frac{\delta}{\sqrt{4G^2+\delta^2}}$ added to the state. Here *G* represents the matrix element between the two involved states.

5.1 Quantum gates on the encoded qubit

Single qubit rotations $R_x(\vartheta)$ on the encoded qubit can be implemented by a sequence of five rf pulses (three frequencies), as sketched in Fig. S10. In particular, the first two π pulses, resonant with transitions $|m_S = -\frac{1}{2}, \frac{3}{2}\rangle \leftrightarrow |m_S = -\frac{1}{2}, m_I = \frac{1}{2}\rangle$ and $|m_S = -\frac{1}{2}, \frac{1}{2}\rangle \leftrightarrow |m_S = -\frac{1}{2}, m_I = -\frac{1}{2}\rangle$ are used to swap the $|1\rangle$ component of the wave-function to $|m_S = -\frac{1}{2}, m_I = -\frac{1}{2}\rangle$. Then, a pulse of proper duration implements the desired rotation and two final π pulses bring back the $|1\rangle$ component to $|m_S = -\frac{1}{2}, \frac{3}{2}\rangle$.

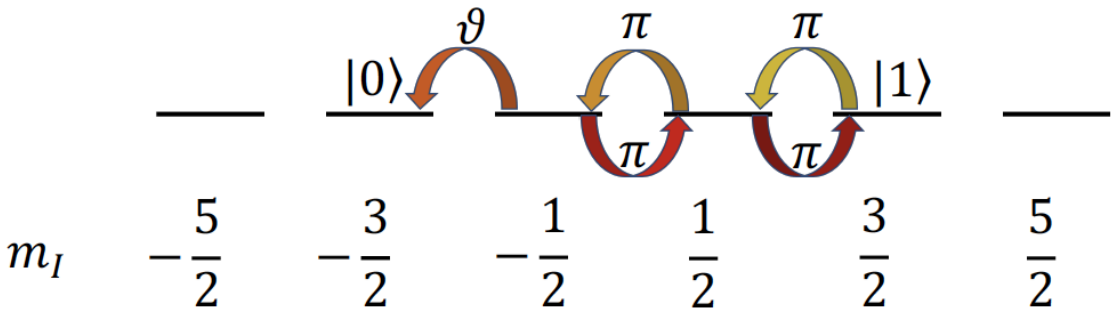

Fig. S10: Implementation of $R_x(\vartheta)$ single qubit rotations on the encoded qubit, by means of rf pulses applied in sequence (from the yellow to the dark red one).

$R_z(\vartheta)$ on the encoded qubit can be easily implemented by a single mw pulse semi-resonant with $|m_S = -\frac{1}{2}, \frac{3}{2}\rangle \leftrightarrow |m_S = \frac{1}{2}, \frac{3}{2}\rangle$ gap, which adds the desired phase only to the $|1\rangle$ component of the wave-function.

5.2 Initialization

Thanks to the large hyperfine interaction provided by RE ions, the lowest gap for $\theta = 0°$ is about 650 MHz = 34 mK above B=0.1 T. Hence we can achieve initialization by cooling, e.g. by means of a dilution refrigerator [S11].

Alternatively, the electronic spin can be exploited to initialize the nuclear qubits in a pure state by algorithmic cooling [S12].

Supplementary References

S1. Pedersen, K. S.; Ungur, L.; Sigrist, M.; Sundt, A.; Schau-Magnussen, M.; Vieru, V.; Mutka, H.; Rols, S.; Weihe, H.; Waldmann, O.; Chibotaru, L. F.; Bendix, J.; Dreiser, J. *Chem. Sci.* **2014**, *5*, 1650.

S2. (a) Pedersen, K. S.; Dreiser, J.; Weihe, H.; Sibille, R.; Johannesen, H. V.; Sorensen, M. A.; Nielsen, B. E.; Sigrist, M.; Mutka, H.; Rols, S.; Bendix, J.; Piligkos, S. *Inorg. Chem.* **2015**, *54*, 7600. (b) Pedersen, K. S.; Ariciu, A.-M.; McAdams, S. G.; Weihe, H.; Bendix, J.; Tuna, F.; Piligkos, S. *J. Am. Chem. Soc.* **2016**, *138*, 5801.

S3. Allodi, G.; Banderini, A; De Renzi, R. *Rev. Sci. Instruments* **2005**, *76*, 083911.

S4. Hahn, E. L. *Phys. Rev.* **1950**, *80*, 580.
S5. Slichter, C. P. *Principles of Magnetic Resonance*; 3rd ed., Springer 1990, Chapter 8, page 367-371.
S6. Narath, A. *Phys. Rev.* **1967**, *162*, 320.
S7. Pirandola, S.; Mancini, S.; Braunstein, S. L.; Vitali, D. *Phys. Rev. A* **2008**, *77*, 032309.
S8. Gottesman, D.; Kitaev, A.; Preskill, J. *Phys. Rev. A* **2001**, *64*, 012310.
S9. Brennen, G. K.; O'Leary, D. P.; Bullock, S. S. *Phys. Rev. A* **2005**, *71*, 052318.
S10. Merkel, S.T.; Jessen, P. S.; Deutsch, I. H. *Phys. Rev. A* **2008**, *78*, 023404.
S11. Song, Y. J.; Otte, A. F.; Shvarts, V.; Zhao, Z.; Kuk, Y.; Blankenship, S. R.; Band, A.; Hess, F. M.; Stroscio, J. A. *Rev. Sci. Instruments* **2010**, *81*, 121101.
S11. Park, D. K.; Feng, G.; Rahimi, R.; Labruyère, S.; Shibata, T.; Nakazawa, S.; Sato, K.; Takui, T.; Laflamme, R.; Baugh, J. *Quantum Inf. Process* **2015**, 14, 2435.